Site-Selective Heat Boosting Electrochemiluminescence for Single Cell Imaging

Xiaodan Gou, Yiwen Zhang, Zejing Xing, Cheng Ma,* Changjie Mao,* Jun-Jie Zhu,*.

ABSTRACT: In operando visualization of local electrochemical reactions provides mechanical insights into the dynamic transport of interfacial charge and reactant/product. Electrochemiluminescence is a crossover technique that quantitatively determines faraday current and mass transport in a straightforward manner. However, the sensitivity is hindered by low collision efficiency of radicals and side reactions at high voltage. Here, we report a site-selective heat boosting electrochemiluminescence microscopy. The luminescence intensity was enhanced up to 63 times and the applied voltage was advanced by 0.2 V thanks to a micron scale heat point in situ generated at electrode-solution interface. Experimental results and finite element simulation demonstrate that the fundamental reasons are accelerated reaction rate and thermal convection via photothermal effect. The concentrated electrochemiluminescence not only boosts the contrast of single cells by 20.54 times but also enables the site-selective cell-by-cell analysis for the heterogeneous membrane protein abundance. This electrochemical visualization method has great potential in highly sensitive and selective analysis of local electron transfer occurred in organism and catalyst.

1

Table of Contents

Chemicals and reagents

Unless otherwise stated, all chemicals and reagents were used as received without further purification. Ultrapure water with a resistivity of 18.2 MΩ·cm was produced by using a Milli-Q apparatus (Millipore) and used in the preparation of all solutions. Tris(2,2′-bipyridyl) dichlororuthenium (II) hexahydrate ($Ru(bpy)_3Cl_2$), tripropylamine (TPrA), 1-ethyl-3-(3-dimethylaminopropyl) carbodiimide (EDC), 1.5 μm and 5 μm micro particles based on silicon dioxide (SiO_2 balls), and 10 μm carboxylated polystyrene (PS) microspheres were purchased from Sigma-Aldrich. Tris(2,2'-bipyridine)ruthenium-bis(hexafluorophosphate) ($Ru(bpy)_3PF_6$), branched polyethyleneimine (PEI, MW = 600), tetraethylorthosilicate (TEOS), bis(2,2'-bipyridine)-4'-methyl-4-carboxybipyridine-ruthenium N-succinimidyl ester-bis(hexafluorophosphate) ($Ru(bpy)_2(mcbpy-O-Su-ester)(PF_6)_2$), sulfosuccinimidyl biotin (sulfo-NHS-biotin), Cetrimonium tosylate (CTAT) and Triethanolamine (TEA) were purchased from Aladdin Reagent Inc. Triton X-100 was purchased from Macklin Biochemical Co., Ltd. 4% paraformaldehyde solution, phosphate buffer solution for cell culture (PBS, 100 mM, pH 7.3), phosphate buffer solution (PBS, 10 Mm, pH 7.4) and Roswell Park Memorial Institute 1640 medium (RPMI-1640, containing 2.0 mg/mL D-glucose, 0.3 mg/mL glutamine, 2.0 mg/mL $NaHCO_3$, 80 U/mL penicillin, and 0.08 mg/mL streptomycin) were purchased from KeyGEN BioTECH. Dimethyl sulfoxide (DMSO, 99.9%, SuperDry, J&KSeal) was obtained from J&K Scientific (Shanghai, China). ITO was purchased from Zhongjingkeyi Technology Co., Ltd. Prior to use, glassy carbon electrodes (GCE) and gold electrodes (3 mm in diameter) were polished sequentially with 1, 0.3 and 0.05 μm alumina powder on a suede cloth, then ultrasonic cleaned with ethanol and ultrapure water twice. At last, the electrodes were dried under a N_2 flow.

Cell culture and labeling for imaging

A CEM cell line were purchased from the Institute of Cell Biology at the Chinese Academy of Sciences (Shanghai, P. R. China) and cultured in RPMI-1640 medium at 37 °C under 5% CO_2 atmosphere for 24h. Prior to experiment, the cell culture medium was discarded and cells were rinsed twice with PBS. For non-labeling ECL imaging, CEM cells would be placed on the GCE and fixed with paraformaldehyde for 10 min. Subsequently, the solution was discarded and cells were rinsed twice with PBS, followed by adding PBS solution containing luminophore $Ru(bpy)_3Cl_2$ and coreactant TPrA (or just TPrA). The labeling of CEM cell was partly referenced to the previous literature.[1] Briefly, a solution of 100 μL ruthenium complex (10 mg/mL) in anhydrous DMSO, 100 μL streptavidin (1mg/mL in PBS), and 400 μL PBS was mixed for 4 h and subsequently dialyzed overnight at 4 °C. The CEM cells in PBS solution were then centrifuged at 1000rpm for 5 min, mixed with PBS solution containing 5 mg/ml sulfo-NHS-biotin and reacted for half an hour at 4 °C. Before ECL imaging, the biotin labeled CEM cells were rinsed with cold PBS twice and placed on the GCE, fixed by paraformaldehyde for 10 min, labeled with streptavidin-ruthenium complex solution SA@Ru (0.1 mg/mL) for 1 h.

Synthesis of RuDSNs

The RuDSNs were prepared as previously reported.[2] Briefly, 1.77 mL of Triton X-100 was dispersed into 1.8 mL n-hexanol and 7.5 mL cyclohexane under stirring for 10 minutes. Then, 340 mL of 0.04 M $Ru(bpy)_3^{2+}$ aqueous solution and 100 mL TEOS was added into the mixture in order. To initiate the polymerization, 60 mL $NH_3 \cdot H_2O$ was added after 5 minutes. The reaction was left for 24 h at 25 °C with gentle stirring. Then, 2 mL acetone was added and the solution was sonicated for another 1 h. After carefully washing with ethanol twice to remove extra $Ru(bpy)_3^{2+}$ and residual surfactant molecules, the precipitation was dispersed in 10 ml ethanol.

Synthesis of MSN

MSN were synthesized according to the previous report.[3] 0.17 g TEA with 1.0 g CTAT were stirred at 80 °C for 1h in 50 ml water. Subsequently, the TEOS of 2 mL was added and stirred for another 2h. After washing three times with ethanol, MSN were dried in oven at 60 °C overnight.

Synthesis of NCDs/MSN

NCDs were synthesized according to a previously reported hydrothermal method.[4] Briefly, 10 mL PEI (280 mg/mL) aqueous solution was heated at 180 °C for 4 h in a 50 mL Teflon-lined stainless-steel autoclave. When cooled down to room temperature, the sample was dialyzed against distilled water using dialysis membranes (MWCO = 10 kDa) for 3 days. Finally, the sample was lyophilized and stored at 4 °C. Prior to experiment, the NCDs were mixed with 1 mg/ml MSN overnight to get NCDs/MSN through electrostatic attraction.

3

Synthesis of Ru(bpy)₃²⁺ labeled beads

For 1.5 μm and 5 μm $Ru(bpy)_3^{2+}$ labeled SiO_2 beads, firstly, 20 mg purchased SiO_2 beads were dispersed into anhydrous ethanol, followed by the addition of 500 mg of $Ru(bpy)_3Cl_2$. In the presence of 100 μL concentrated ammonia solution, 14.8 μL of TEOS was added to the solution in portions, vigorously stirred, and allowed to react for 20 hours. The resulting yellow solid was centrifuged and washed three times with ethanol. Subsequently, the solid was dispersed in ethanol for further use. For 10 μm carboxylated PS microspheres, which possess abundant carboxyl groups on their surface, 10 μL of the PS microspheres were centrifuged and dispersed in DMSO. Then, 5 mg of Ru-NHS and 40 mg EDC was added to the solution, and the mixture was stirred at room temperature for 2 hours. Subsequently, the mixture was centrifuged at 3000 rpm and dispersed in DMSO for future use.
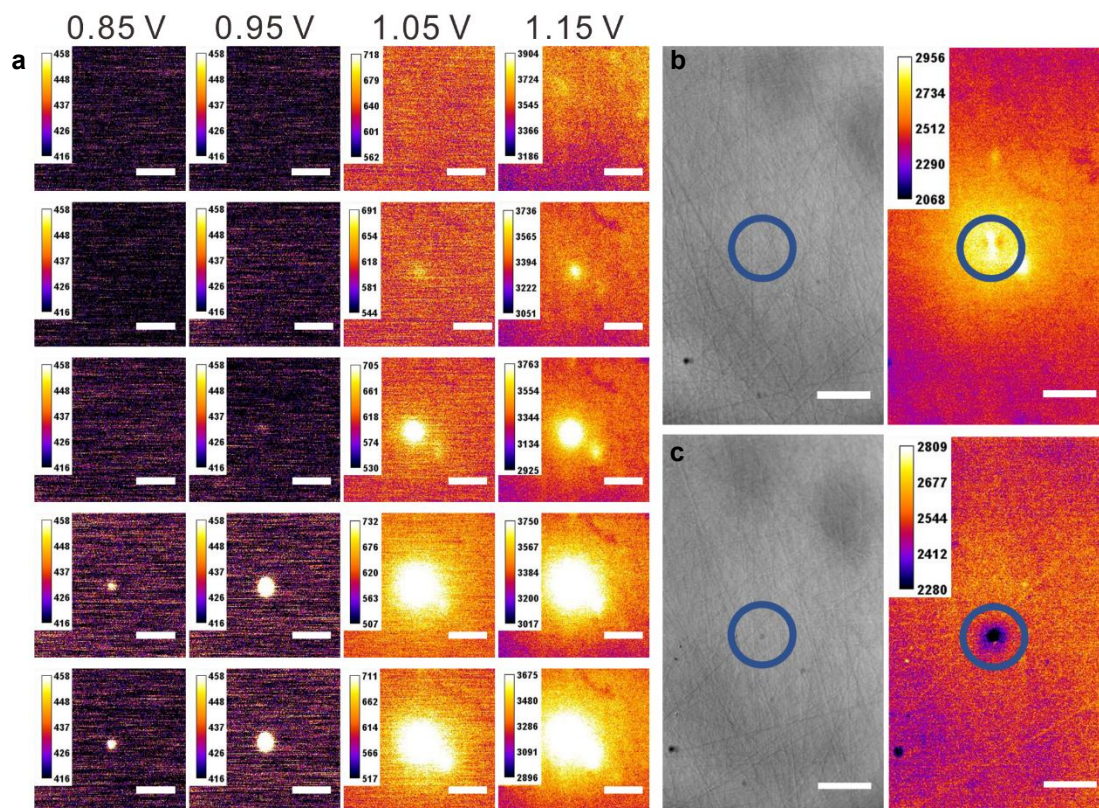
Results and Discussion

Table S1. The corresponding power density of laser and the current shown in current controller

Current (mA)	Power density ($\mu W/\mu m^2$)	Current (mA)	Power density ($\mu W/\mu m^2$)
1	0.0018	50	49.44
5	0.0175	55	164.9
10	0.0470	60	189.0
15	0.0950	65	204.4
30	01845	70	331.6
25	0.3709	75	385.9
30	0.9648	80	521.6
35	8.653	85	687.4
40	22.85	90	750.7
45	36.18	100	783.9

Figure S1. (a) HT-ECL images of different laser power density at the applied potential from 0.85 V to 1.15 V, scan rate: 10 mV/s. The corresponding laser power densities of the images from top to bottom are 0.9648 (30 mA), 8.653 (35 mA), 22.85 (40 mA), 36.18 (45 mA), 49.44 (50 mA) $\mu W/\mu m^2$, respectively. The electrolyte is 10 mM PBS solution (pH 7.4) containing1 mM Ru(bpy)$_3^{2+}$ and 100 mM TPrA. Exposure time: 200 ms. Scale bar (white) is 10 μm.(b) The BF image (left) and the HT-ECL image (right) at the constant potential of 1.2 V with the laser power density of 164.9 $\mu W/\mu m^2$ (55 mA). The electrolyte is the same as that in (a). Exposure time: 200 ms. Scale bar (white) is 20 μm. (c) The BF image (left) and the ECL image at 1.2 V (right) after illuminated by the power density of 189.0 $\mu W/\mu m^2$ (60 mA). At this time, the laser region showing a black burn mark during the ECL process, which could also be noticed in BF. Exposure time: 200 ms. Scale bar (white) is 20 μm.

Table S2. The gain under the laser power from 30 mA 0.9648 ($\mu W/\mu m^2$) to 50 mA (49.44 $\mu W/\mu m^2$) at 0.95 V

| Laser current (mA)	30	35	40	45	50
Gain	/	/	1.74	31.91	63.75

As shown in Figure S1 and table S2, when the power density of laser was 0.9648 $\mu W/\mu m^2$ (30 mA), the HT-ECL did not happen. The HT-ECL could be observed when laser power increased to 8.653 and 22.85 $\mu W/\mu m^2$ (35 and 40 mA), but the potential advance was absence at this time. When the power density reached 36.18 $\mu W/\mu m^2$ (45 mA) and 49.44 $\mu W/\mu m^2$ (50 mA), HT-ECL phenomenon of enhancing local ECL intensity and advancing trigger ECL potential could be discovered. However, when the power density was over 164.9 $\mu W/\mu m^2$ (55 mA), the HT-ECL region appeared black spots, implying the possibility to damage the GCE surface. At this time, the region burned by laser could not be seen in BF image. But when power density achieved 189.0 $\mu W/\mu m^2$ (60 mA), the burn mark could be clearly identified in BF images. Based on this optimization, we chose 36.18 to 49.44 $\mu W/\mu m^2$ (45 to 50 mA) as experimental power density. Noted, all the power density below 331.6$\mu W/\mu m^2$ (70 mA) could not be collected by EMCCD camera with the exposure time of 200 ms.
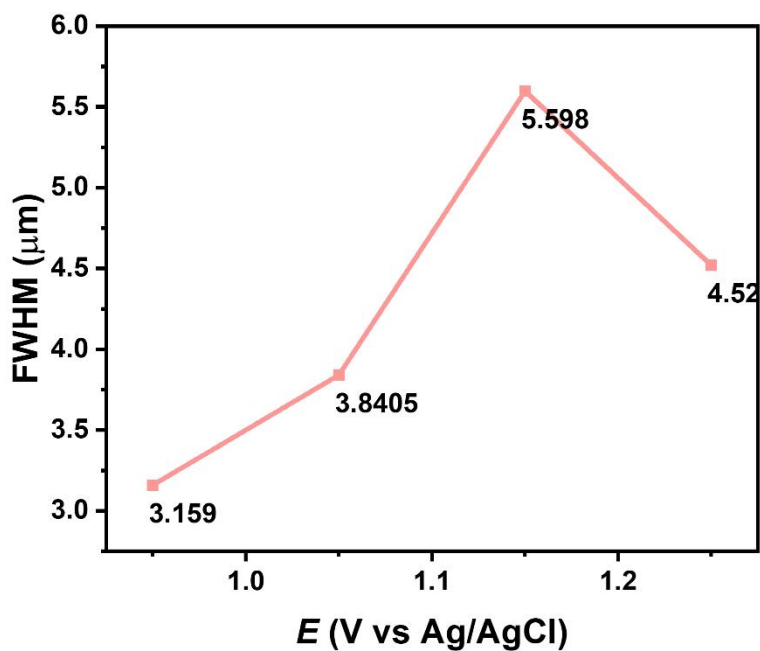
96
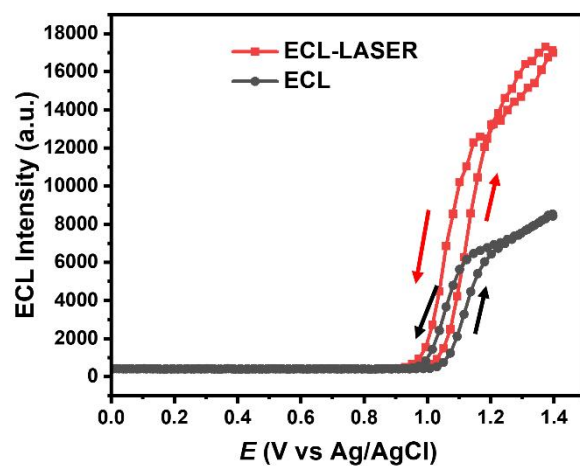
Figure S2. ECL and HT-ECL-potential curves in 10 mM PBS solution (pH 7.4) containing 1 mM Ru(bpy)$_3^{2+}$ and 100 mM TPrA. Scan
range from 0 V to 1.4 V, and scan rate: 10 mV/s.

As shown in Figure S2, the HT-ECL exhibited the higher ECL emission during applying potential from 0 to 1.4 V.
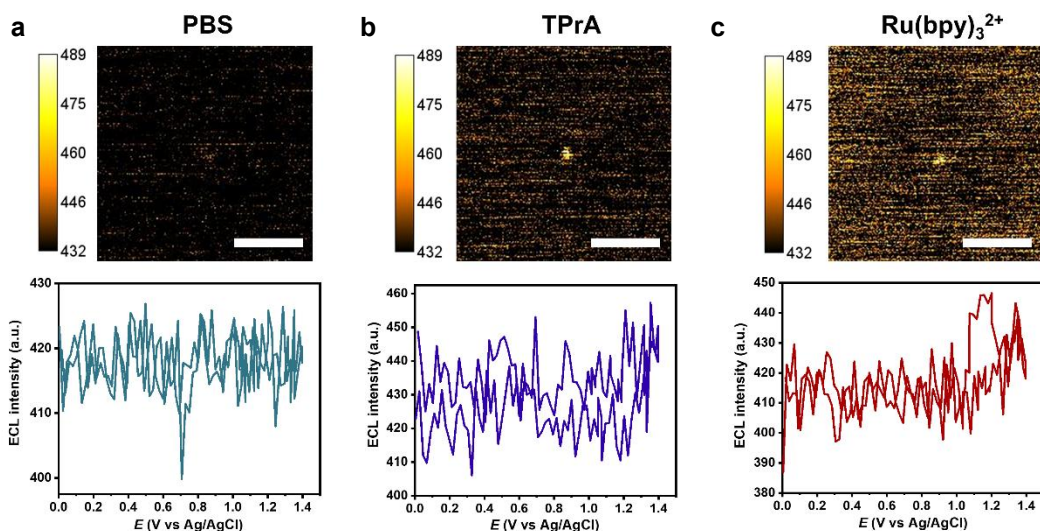
100

101

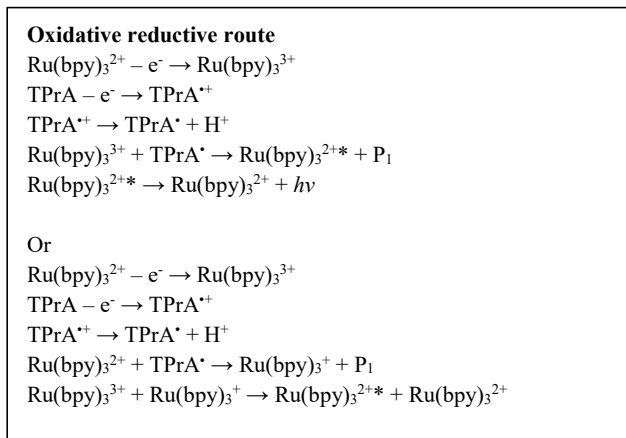Figure S3. The FWHM varies as the voltage changes.

103

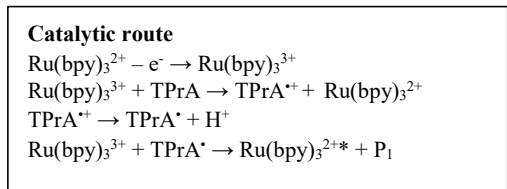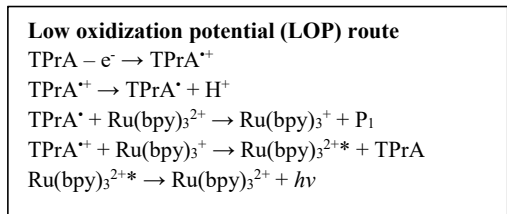104

105

Figure S4. The corresponding laser spot images and intensity curves along the radius of laser spot in 10 mM PBS (a), 100 mM TPrA (b), 1 mM $Ru(bpy)_3^{2+}$ (c), respectively. The applied potential was cyclically from 0 V to 1.4 V at the scan rate of 10 mV/s. Scale bar (white) is 20 μm. Exposure time: 200 ms.

**Low oxidization potential (LOP) route**

$TPrA - e^- \rightarrow TPrA^{\bullet+}$

$TPrA^{\bullet+} \rightarrow TPrA^{\bullet} + H^+$

$TPrA^{\bullet} + Ru(bpy)_3^{2+} \rightarrow Ru(bpy)_3^+ + P_1$

$TPrA^{\bullet+} + Ru(bpy)_3^+ \rightarrow Ru(bpy)_3^{2+*} + TPrA$

$Ru(bpy)_3^{2+*} \rightarrow Ru(bpy)_3^{2+} + h\nu$

Catalytic route

$Ru(bpy)_3^{2+} - e^- \rightarrow Ru(bpy)_3^{3+}$

$Ru(bpy)_3^{3+} + TPrA \rightarrow TPrA^{\bullet+} + Ru(bpy)_3^{2+}$

$TPrA^{\bullet+} \rightarrow TPrA^{\bullet} + H^+$

$Ru(bpy)_3^{3+} + TPrA^{\bullet} \rightarrow Ru(bpy)_3^{2+*} + P_1$

Oxidative reductive route

$Ru(bpy)_3^{2+} - e^- \rightarrow Ru(bpy)_3^{3+}$

$TPrA - e^- \rightarrow TPrA^{\bullet+}$

$TPrA^{\bullet+} \rightarrow TPrA^{\bullet} + H^+$

$Ru(bpy)_3^{3+} + TPrA^{\bullet} \rightarrow Ru(bpy)_3^{2+*} + P_1$

$Ru(bpy)_3^{2+*} \rightarrow Ru(bpy)_3^{2+} + h\nu$

Or

$Ru(bpy)_3^{2+} - e^- \rightarrow Ru(bpy)_3^{3+}$

$TPrA - e^- \rightarrow TPrA^{\bullet+}$

$TPrA^{\bullet+} \rightarrow TPrA^{\bullet} + H^+$

$Ru(bpy)_3^{2+} + TPrA^{\bullet} \rightarrow Ru(bpy)_3^+ + P_1$

$Ru(bpy)_3^{3+} + Ru(bpy)_3^+ \rightarrow Ru(bpy)_3^{2+*} + Ru(bpy)_3^{2+}$

Scheme S1. Typical routes for ECL reactions in $Ru(bpy)_3^{2+}$ and TPrA as coreactant. For the CEM cells labeling experiment, the LOP reaction route dominates. P1 is short for $Pr_2N^+=CHCH_2CH_3$.
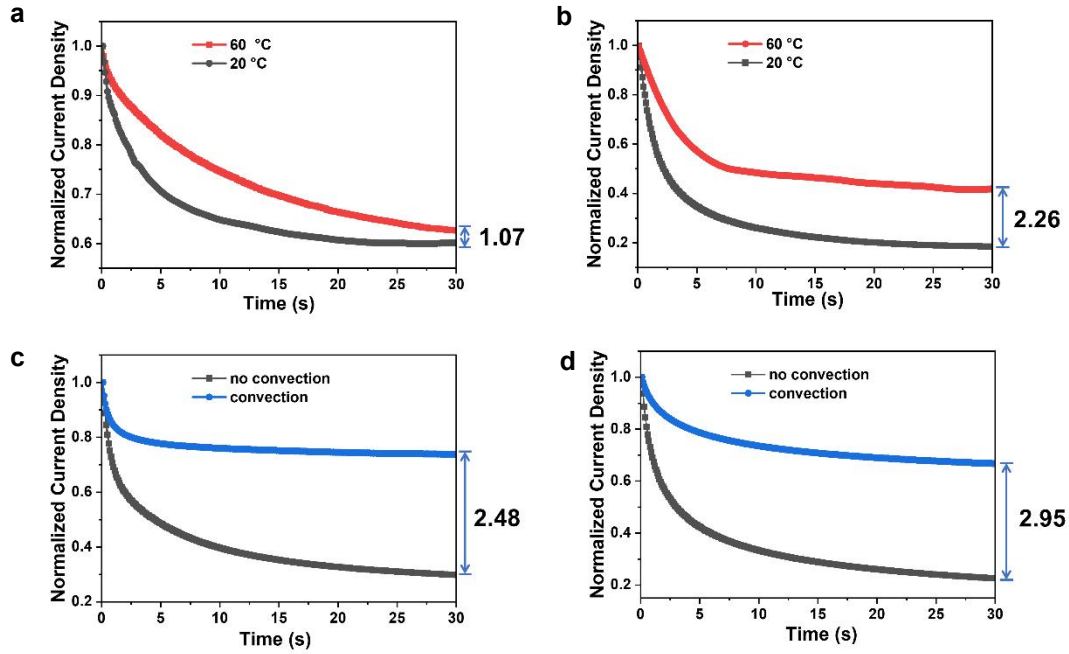
Figure S5. (a)-(b) The normalized current density diagrams of Ru(bpy)$_3^{2+}$ (a), TPrA (b) at 60°C and 20 °C. (c)-(d) The normalized current density of Ru(bpy)$_3^{2+}$ (c), TPrA (d) without and with convection speed of 1314 rpm. The applied potential was 1.3 V.

According to the direct observation of thermal convection (refer to main text, Figure 3), we estimated the convection speed at the place of 10 μm around the laser spot is 8.23 μm/s. The convection speeds of rotating disk electrode (RDE) are described as[5]:

$$v_y = -0.51\omega^{3/2}\nu^{-1/2}y^2 \tag{eq S1}$$

$$v_r = 0.51\omega^{3/2}\nu^{-1/2}ry \tag{eq S2}$$

Where v_y is the speed in the vertical direction, v_r is the radial velocity, y is the vertical distance and r is the radial distance to the center of the disk, and ω is the angular velocity or rotation speed of the disk. ν for water is 0.01 cm^2/s. Here, we assumed y=1 μm and r=10 μm. By substituting v_r=8.23 μm/s into eq S2, the corresponding ω can be determined as 137.6 s^{-1}. Thus, the rotation speed n=ω/2π was calculated as 21.9 r/s, equivalent to 1314 rpm.

COMSOL simulation

COMSOL Multiphysics (Version 5.6) was employed to simulate the locally heating process and the ECL changing related to temperature gradient. The whole digital simulation was divided into two parts: Heat transfer process and the ECL reaction process.

For the heat transfer process, the incident heat flux from laser was modeled as the heat source distributed on the electrode surface. A set of variables were introduced to define the Gaussian distribution of the heat load around the irradiation place (eq S3). Assuming that good thermal isolation from the environment was achieved and the ambient temperature was 20 °C, and the absorptivity equaled emissivity, thus the heat load from laser needed to multiply the emissivity (eq S4). Also, assuming that the electrode was not transparent at the wavelength of laser, all the heat generated by laser was deposited on the surface. The power density of laser was according to table S1, choosing 36.18 μW/μm^2 (45 mA) as representative. The radius of laser spot (r_spot) was measured as 3.25 μm by ECLM. The emissivity of glassy carbon was referenced to the previous paper.[6]

$$\text{Flux} = ((2 \cdot \text{p\_laser})/(\pi \cdot \text{r\_spot}^2)) \cdot \exp(-(2 \cdot \text{r\_focus}^2)/\text{r\_spot}^2) \tag{eq S3}$$

r_focus represented for the distance to the laser irradiation place, the value of p_laser could be found in table S3.

$$Q = \text{emissivity} \cdot \text{Flux} \tag{eq S4}$$

"Heat transfer in solids" physical field was used for modeling the process of laser locally heating the electrode. In this physical field, the conductive heat flux q could be described by Fourier's law as below, proportional to the temperature gradient:

$$q = -k\nabla T$$

143   For the time-dependent study, the temperature field in the immobile solids followed the heat equation:

$$\rho C_p \frac{\partial T}{\partial t} = \nabla \cdot (k\nabla T) + Q$$

144   **Table S3. Parameters of heat transfer process.**

Name	Value	Description
r_spot	3.25×10^{-6} m	The radius of laser spot
emissivity	0.8	The surface emissivity of glassy carbon
p_laser	0.0012 W	The laser power

145

146   Subsequently, the laminar flow module coupling with gravity field was added to simulate the heat conduction. As shown in
147   Figure S9, it is sufficient to cause heat convection near the electrode surface at this temperature difference.

148   For the ECL reaction process, only the main ECL routes were considered due to the complicated mechanisms. The reaction
149   equations are as follows:

150   Heterogeneous electron transfer reactions:

151    $\text{Ru(bpy)}_3^{2+} \xrightarrow{k_1} \text{Ru(bpy)}_3^{3+} + e^-$ (eq S5)

152    $\text{TPrA} \xrightarrow{k_2} \text{TPrA}^{\bullet+} + e^-$ (eq S6)

153    $\text{TPrA}^{\bullet} \xrightarrow{k_3} P1 + e^-$ (eq S7)

154   Homogeneous reactions:

155    $\text{TPrAH}^+ \xrightarrow{k_4} \text{TPrA} + H^+$ (eq S8)

156    $\text{TPrA}^{\bullet+} \xrightarrow{k_5} \text{TPrA}^{\bullet} + H^+$ (eq S9)

157    $\text{Ru(bpy)}_3^{3+} + \text{TPrA}^{\bullet} \xrightarrow{k_6} \text{Ru(bpy)}_3^{2+*} + P1$ (eq S10)

158    $\text{Ru(bpy)}_3^{3+} + \text{TPrA} \xrightarrow{k_7} \text{Ru(bpy)}_3^{2+} + \text{TPrA}^{\bullet+}$ (eq S11)

159    $\text{Ru(bpy)}_3^{2+*} \xrightarrow{k_8} \text{Ru(bpy)}_3^{2+} + h\nu$ (eq S12)

160

161

162   **Table S4. The reaction rates of ECL process.**

Domain	Name	Value	Description
Electrode surface (heterogeneous reaction)	k1	15 cm/s	Rate constant of eq. S5
	k2	10^{-4} m/s	Rate constant of eq. S6
	k3	10^{-4} m/s	Rate constant of eq. S7
Electrolyte (homogeneous reaction)	k4	8 1/s	Rate constant of eq. S8
	k5	3500 1/s	Rate constant of eq. S9
	k6	10^6 m³/(s*mol)	Rate constant of eq. S10
	k7	13 m³/(s*mol)	Rate constant of eq. S11

9

	k8	300 1/s	Rate constant of eq. S12

163

"Transport of Diluted Species" physical field was chosen to simulate the ECL process. In this physical field, the time-dependent transport of dilute species followed the equation below:

$$\nabla \cdot \left(- D_i \nabla c_i \right) + \mathbf{u} \cdot \nabla c_i = R_i$$

As mentioned before, the ECL reactions could be divided into two categories: heterogeneous electron transfer reactions on the electrode surface and the homogeneous reactions in the electrolyte domain. The effect of temperature would be discussed following this classification.

On the electrode surface, the flux (J) boundaries could be simulated as:

$$J_{Ru^{2+}} = -J_{Ru^{3+}} = - k_1[Ru^{2+}] \qquad \text{(eq S13)}$$

$$J_{TPrA} = -J_{TPrA^{\bullet+}} = - k_2[TPrA] \qquad \text{(eq S14)}$$

$$J_{TPrA^{\bullet}} = -J_{P1} = - k_3[TPrA^{\bullet}] \qquad \text{(eq S15)}$$

where $[Ru^{2+}]$, $[TPrA]$ and $[TPrA^{\bullet}]$ are the concentrations of Ru(bpy)$_3^{2+}$, $TPrA$ and $TPrA^{\bullet}$, respectively.

According to Butler-Volmer equation,[7] the reaction rates on the electrode could be written as:

$$k = k^0 \exp[(1 - \alpha)(E - E^0)F/RT] \qquad \text{(eq S16)}$$

Where k^0 denotes for the standard rate constant, E the electrode potential set as 1.2 V, E^0 the formal potential which is 1.05 V for Ru(bpy)$_3^{2+}$/Ru(bpy)$_3^{3+}$ and 0.90 V for TPrA oxidization. α is the transfer coefficient, which is taken as 0.5, and the other parameters are: R=8.31 J/(kmol)，F=96485 C/mol. In this equation, the electrode reactions could be linked to the temperature since k_1 at $T_1 = 293$ K was found in previous reports.[8] Thus, it could be deduced as eq S16. By adding the interpolation function, the correlation with temperature could be achieved.

$$k = k_1 \exp\left[(1 - \alpha)(E - E^0)(\tfrac{1}{T} - \tfrac{1}{T_1})F/R\right] \qquad \text{(eq S17)}$$

In the electrolyte domain, if temporarily disregarding the effect of convection, the transition of all ECL species followed the Fick's second low:

$$\frac{\partial C_i}{\partial t} = D_i \nabla^2 C_i \qquad \text{(eq S18)}$$

Thus, the concentration change of ECL species could be described in the following form (table S5):

Table S5. The time-dependent concentration changes of ECL species.

Description	Expression
The concentration change of Ru^{3+}	$\frac{\partial[Ru^{3+}]}{\partial t} = D_{Ru^{3+}}\Delta[Ru^{3+}] - k_6[Ru^{3+}][TPrA^{\bullet}] - k_7[Ru^{3+}][TPrA]$
The concentration change of Ru^{2+}	$\frac{\partial[Ru^{2+}]}{\partial t} = D_{Ru^{2+}}\Delta[Ru^{2+}] + k_7[Ru^{3+}][TPrA] + k_9[Ru^{2+*}]$
The concentration change of TPrA$^{\bullet}$	$\frac{\partial[TPrA^{\bullet}]}{\partial t} = D_{TPrA^{\bullet}}\Delta[TPrA^{\bullet}] + k_5[TPrA^{\bullet+}] - k_6[Ru^{3+}][TPrA^{\bullet}]$
The concentration change of TPrA$^{\bullet+}$	$\frac{\partial[TPrA^{\bullet+}]}{\partial t} = D_{TPrA^{\bullet+}}\Delta[TPrA^{\bullet+}] - k_5[TPrA^{\bullet+}] + k_7[TPrA][Ru^{3+}]$

10

The concentration change of TPrA	$\dfrac{\partial[\text{TPrA}]}{\partial t} = D_{\text{TPrA}}\Delta[\text{TPrA}] - k_7[\text{TPrA}][\text{Ru}^{3+}] + k_4[\text{TPrAH}^+]$
The concentration change of Ru²⁺*	$\dfrac{\partial[\text{Ru}^{2+*}]}{\partial t} = k_6[\text{Ru}^{3+}][\text{TPrA}^\bullet] - k_8[\text{Ru}^{2+*}]$

Table S6. The parameters of ECL process.

Name	Value	Description
cRu0	1 mol/m3	Initial concentration of Ru(bpy)$_3^{2+}$
cTPrA0	100 mol/m3	Initial concentration of TPrA
cH0	3.98*10-5 mol/m3	Initial concentration of H$^+$
cBuf0	200 mol/m3	Initial concentration of buffer
DRu	5.9*10-9 m2/s	Diffusion coefficient of Ru(bpy)$_3^{2+}$ and its derivative at 20°C
DTPrA	5*10-9 m2/s	Diffusion coefficient of TPrA and its derivative at 20°C
DH	5*10-9 m2/s	Diffusion coefficient of H$^+$ at 20°C
DBuf	5*10-10 m2/s	Diffusion coefficient of buffer at 20°C

For the homogeneous reactions, when the temperature changed, both the diffusion coefficient and reaction rates would change. However, the ECL layer was mainly diffusion-controlled shown by the simulation. When changing the diffusion coefficients, the change of ECL layer would be great enough to neglect the change of reaction rates. Thus, the relationship between temperature and diffusion coefficients (D) was the main consideration. According to Stokes-Einstein equation (eq S19), the change extent of D with temperature should be all the same for ECL species.

$D = kT/6\pi r_i \mathbf{u}$ (eq S19)

where k represents for Boltzmann's constant, r_i is the radius of the diffusing species, and $\mathbf{u}$ is the viscosity of the solution.

Referring to the previous reports[9], we derived the change magnitude of diffusion coefficient using 20 °C (known data) as the base (table S7). Likewise, the relationship with temperature could be obtained by setting the interpolation functions according to the data in table S7.

Table S7. The change extent of diffusion coefficient with temperature.

Temperature (°C)	20	30	40	50	60	65
Change extent	1	1.62	2.44	2.98	4.32	4.87

Next, we constructed a 2D axisymmetric geometry (Figure S6), assuming the transport behavior happened vertically above the electrode surface. The mesh setting was extremely fine as shown in Figure S7. As a result, we could obtain the simulation of temperature effect on ECL process without considering the heat convection, which could be found in the main article.
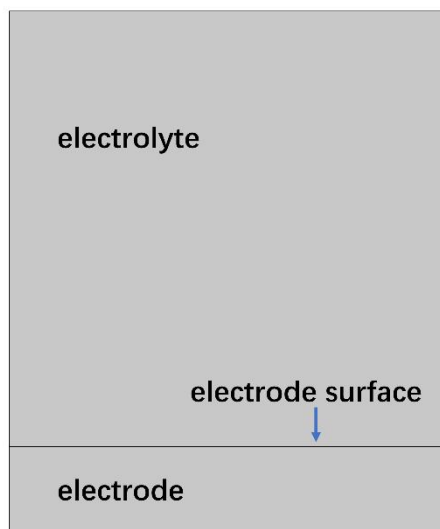
207

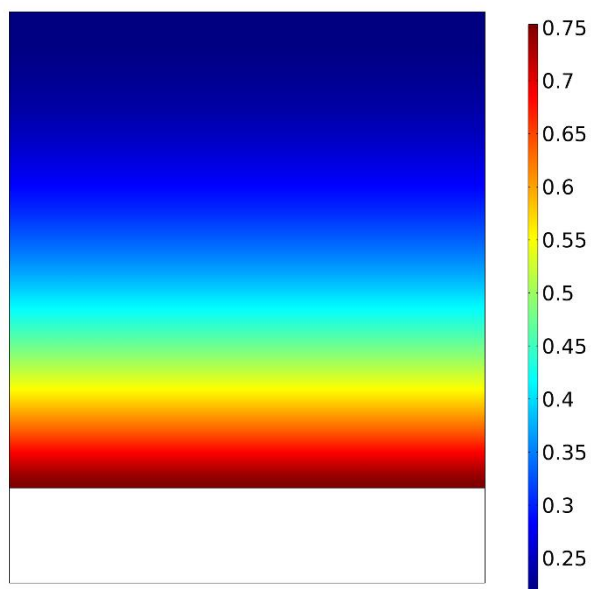208   **Figure S6**. The geometry construction in COMSOL simulation
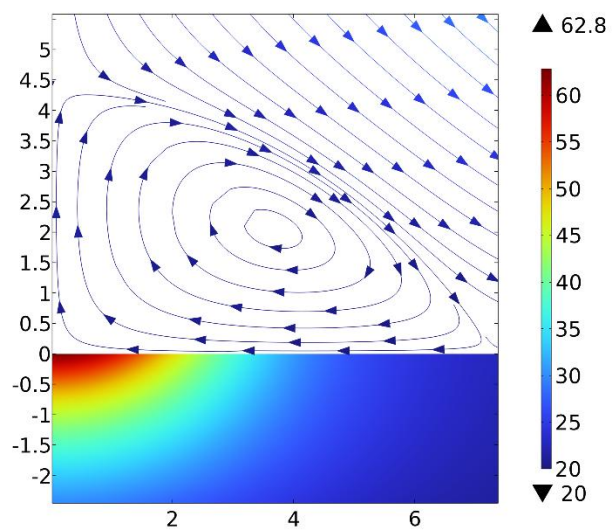
209

210

211

212

213
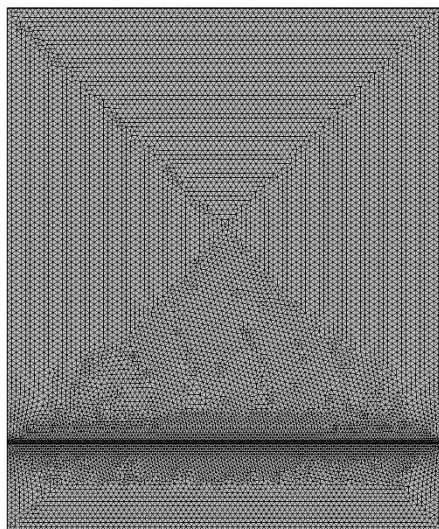
214

215   **Figure S7**. The mesh setting in COMSOL simulation

216

217   **Figure S8**. The Side view image of Ru(bpy)$_3^{2+}$* simulated by COMSOL before considering temperature gradient

218

219   **Figure S9**. The heat convection simulated by COMSOL. The color bar indicates the heat difference on the electrode surface.
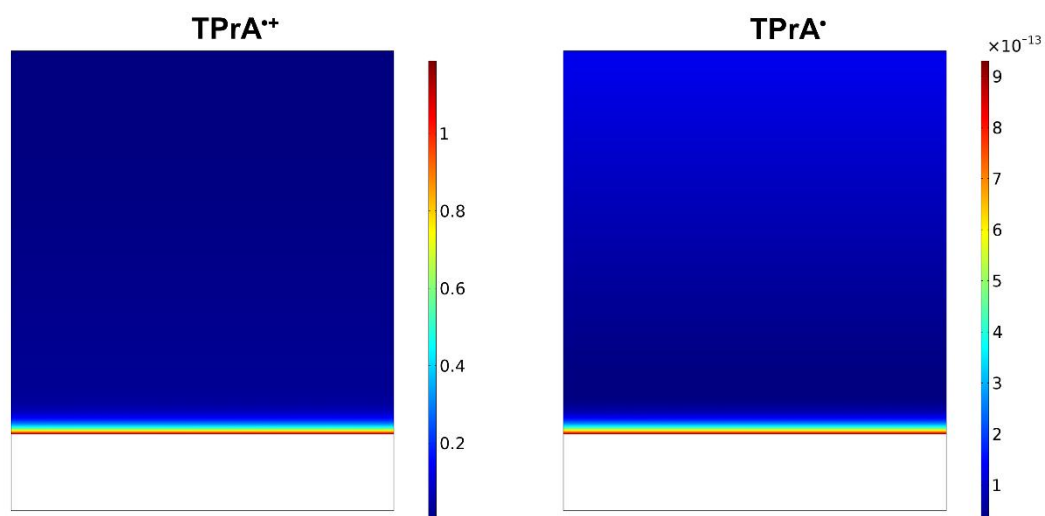
a Change the diffusion coefficient only

b Change the electron transfer rate only
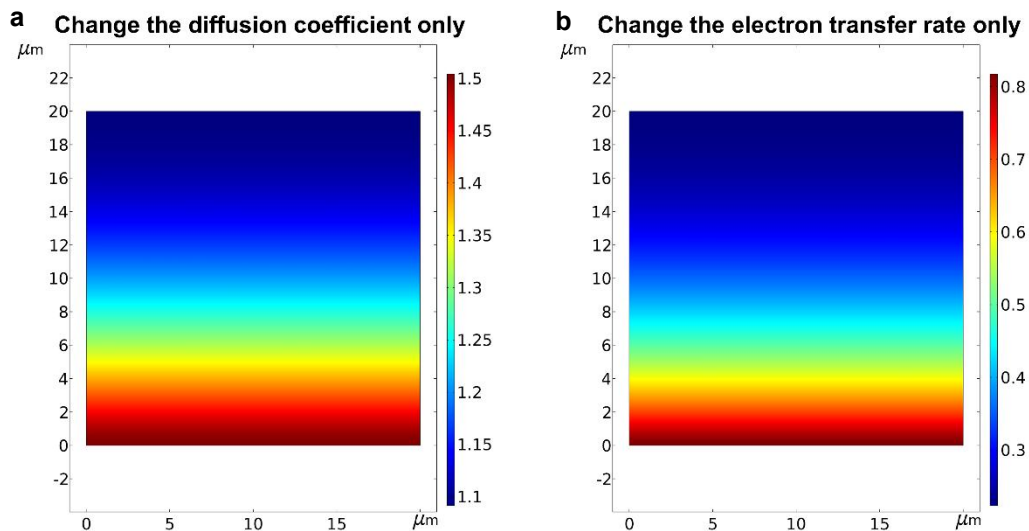
Figure S10. The comparison of simulated Ru(bpy)$_3^{2+}$* distribution between only change the diffusion coefficient at 60 °C (a) and only change the electron transfer rates at 60 °C (b).

TPrA$^{\bullet+}$

TPrA$^{\bullet}$

$\times 10^{-13}$

Figure S11. The concentration of TPrA$^{\bullet+}$ and TPrA$^{\bullet}$ species by COMSOL simulation before considering temperature gradient.

14

228
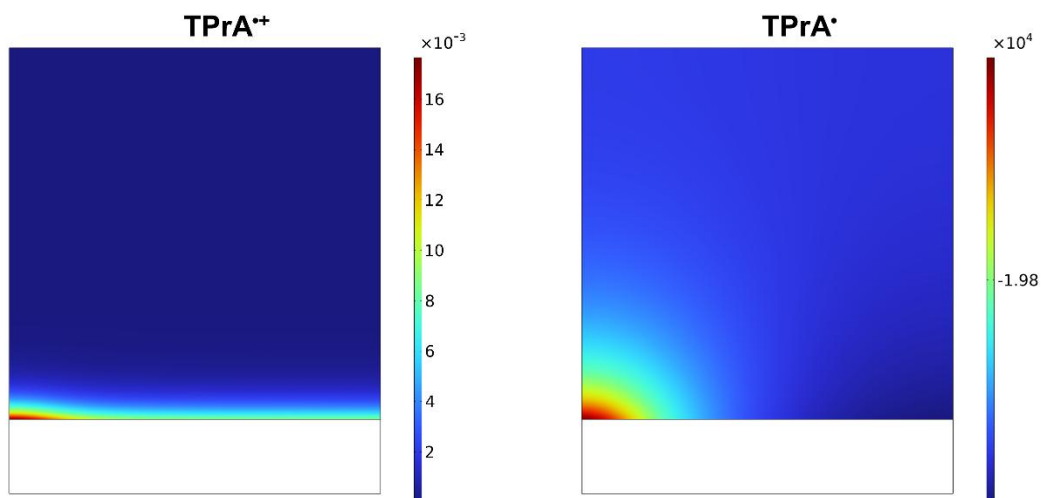
Figure S12. The concentration of TPrA$^{•+}$ and TPrA$^{•}$ species by COMSOL simulation after considering temperature gradient

229

230

231

232
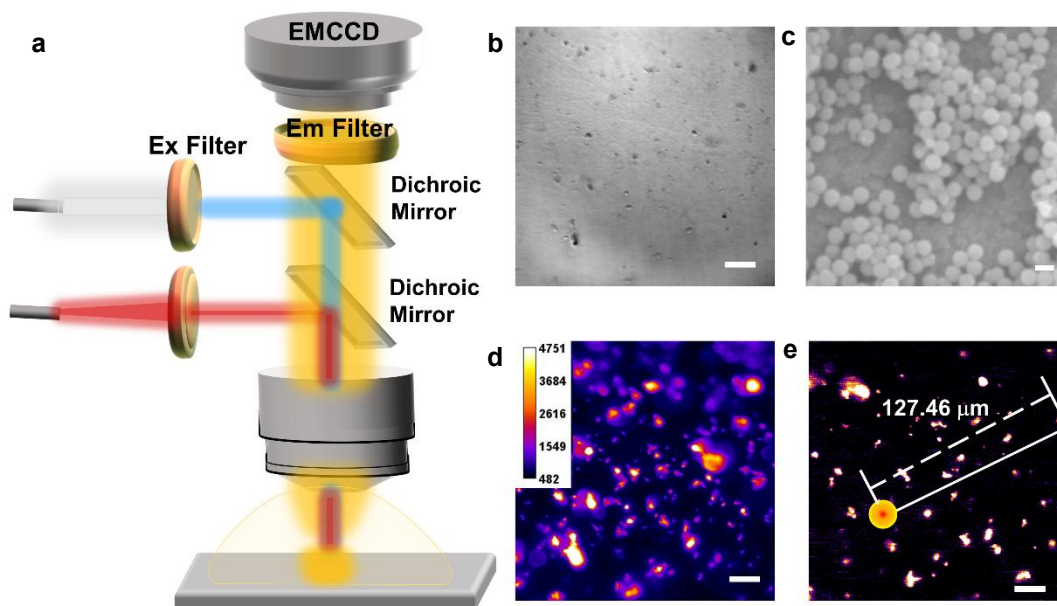
Figure S13. (a) Schematic illustration of the fluorescence collection setup based on ECL microcopy. The lower dichroic mirror could focus the 730 nm laser on the electrode surface. The upper dichroic mirror changes the light source (LED flashlight) into the FL excitation wavelength of RuDSN and allows the FL to penetrate. (b,d) The corresponding BF image (b) and FL image (d) of RuDSN. Scale bar (white) is 20 μm. Exposure time is 10 ms. (c) SEM image of RuDSN. Scale bar (white) is 100 nm. (e) The longest influence range observed of thermal convection is over 127.46 μm. Scale bar (white) is 20 μm. Exposure time is 10 ms.

The SEM image (Figure S13c) of RuDSN displayed nanospheres of good uniformity. The corresponding BF image (Figure S13b) and FL image (Figure S13d) indicated the successful doping of Ru(bpy)$_3^{2+}$ and availability of visualizing thermal convection. The size of RuDSN was around 100 nm in the SEM image, however, inevitable reunion resulted in a bigger size of bright spot in BF and FL images, having no effect on the experimental phenomenon. The detailed microscopy setup for FL images could be seen at experimental section.

15
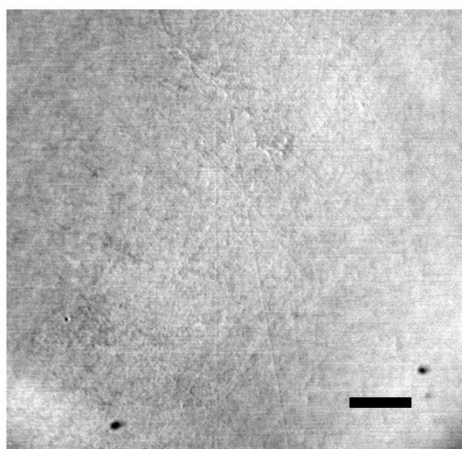
243

244 **Figure S14**. The BF image of Nafion film modified on GCE. Scale bar (black) is 20 μm.

245

246 As seen in Figure S14, the roughness increased compared with the bare GCE, indicating the successful modification of Nafion on
247 GCE surface.

248

249
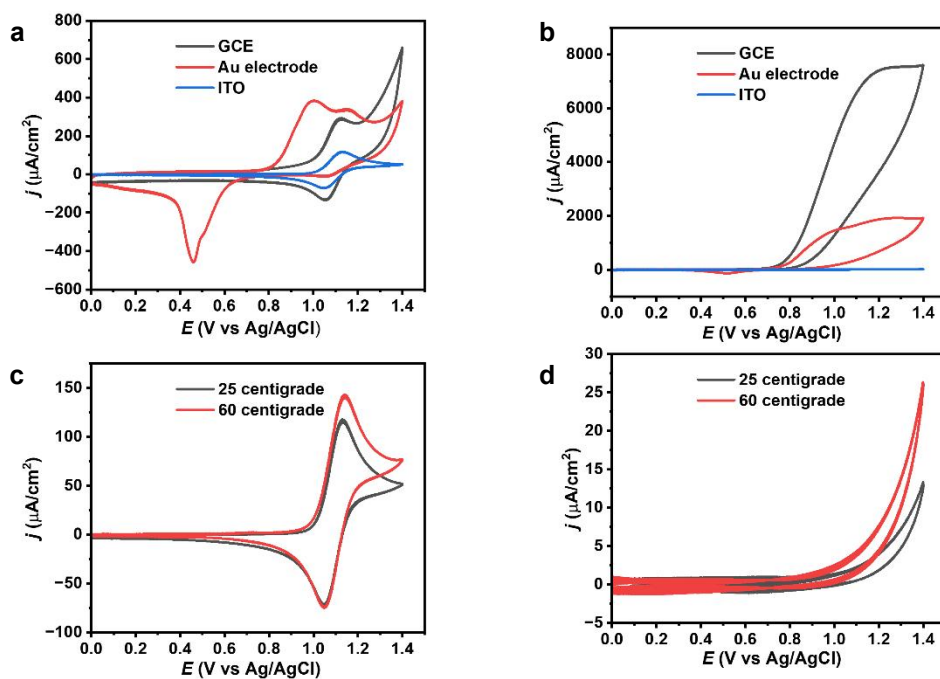
250

251 **Figure S15**. (a) Current density-potential curves of 1 mM Ru(bpy)$_3^{2+}$ on GCE, Au electrode, ITO, respectively. (b) Current density-
252 potential curves of 1mM TPrA on GCE, Au electrode, ITO, respectively. (c) Current density-potential curves of 1 mM Ru(bpy)$_3^{2+}$ on ITO
253 at 25 °C, 60 °C, respectively. (c) Current density-potential curves of 1 mM TPrA on ITO at 25 °C, 60 °C, respectively. The imposed
254 potential was cyclically from 0 V to 1.4 V at the scan rate of 10 mV/s.

255 It is necessary to understand the distinguish between inner-sphere and outer-sphere electron transfer at electrodes, which adopted
256 from the origin of electron transfer of coordination compounds. To be specific, the inner-sphere electron reactions require a sharing

16

257 ion ligand between active compounds, while the "outer-sphere" denotes a reaction between two species in which the original
258 coordination spheres are still maintained. Likewise, the outer-sphere electrode reactions usually take place at the outer Helmholtz
259 plane (OHP) separated by at least a solvent layer from the electrode surface, while the inner-sphere electrode reactions at the inner
260 Helmholtz plane (IHP) through a ligand absorbed on the electrode surface. Thus, the inner-sphere electrode reactions should be
261 more dependent on the electrode materials than the outer-sphere electrode reactions. The previous papers have already indicated the
262 oxidization of $Ru(bpy)_3^{2+}$ is indeed an outer-sphere electrode reaction.[10,11]. We also performed several experiments to confirm the
263 different electron transfer types. First, when changing the electrode from GCE to gold electrode or ITO, it can be seen in Figure
264 S15a, 15b that the oxidization current density of $Ru(bpy)_3^{2+}$ became 1.15 times and 0.32 times than GCE, respectively. The degree
265 of change is much lower than that of TPrA, which the oxidization current density was 0.25 times on gold electrode and 0.0017
266 times on ITO than GCE, respectively. Moreover, we elevated the temperature of ITO to 60 °C. Figure S15c, 15d clearly indicated
267 that the increment in temperature can increase the oxidation current density of $Ru(bpy)_3^{2+}$ to 1.32 times the original, while that of
268 TPrA was 2.03 times, also implying $Ru(bpy)_3^{2+}$ is less susceptible to electrodes than TPrA.
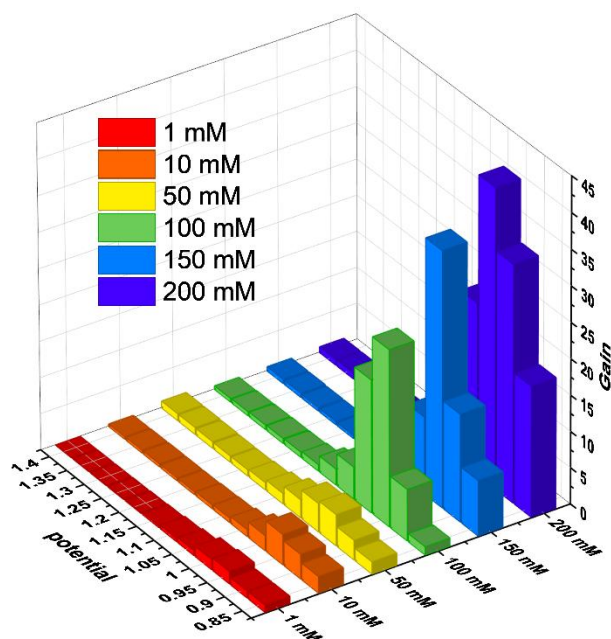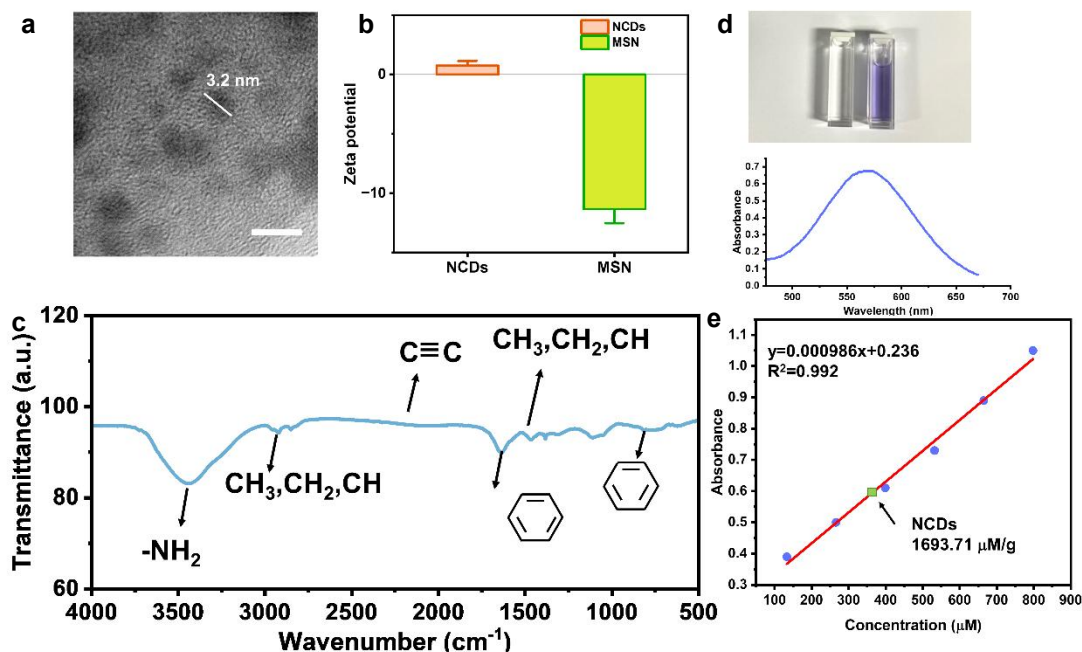
269

270 **Figure S16**. Histogram of gain as a function of applied voltage and TPrA concentration. The applied voltage is from 0 V to 1.4 V at the
271 scan rate of 10 mV/s. The concentration of $Ru(bpy)_3^{2+}$ remains 1 mM.
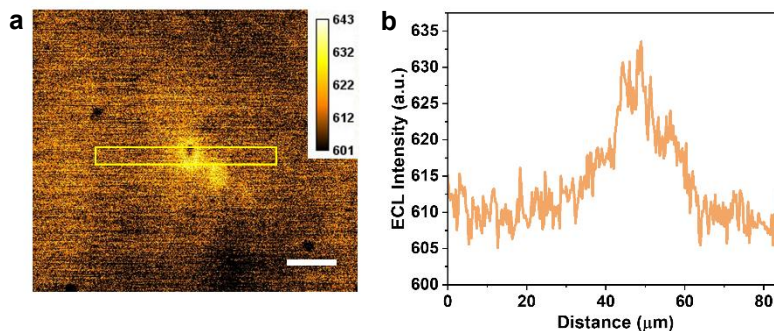
272

273 **Figure S17**. (a) The HT-ECL graph of free NCDs and 1 mM $Ru(bpy)_3^{2+}$ at 1.4 V. (b) The ECL intensity along the yellow block in (a).

274

17

Figure S18. (a) HRTEM image of NCDs. The representative size of NCDs is 3.2 nm. Scale bar (white) is 5 nm. (b) Zeta potential histogram of NCDs and MSN. (c) FT-IR graph of NCDs. (d) The absorbance at 570 nm of Kaiser agent for determining the contents of amino groups in NCDs. Top: The comparison between Kaiser agent (left) and NCDs (right) after reacting with Kaiser agent. Bottom: The absorbance spectra of NCDs with Kaiser agent. (e) The standard curve of amino contents determined by Kaiser agent and glycine. The green square indicates the amino content of NCDs, which was calculated as 1693.71 μM/g.
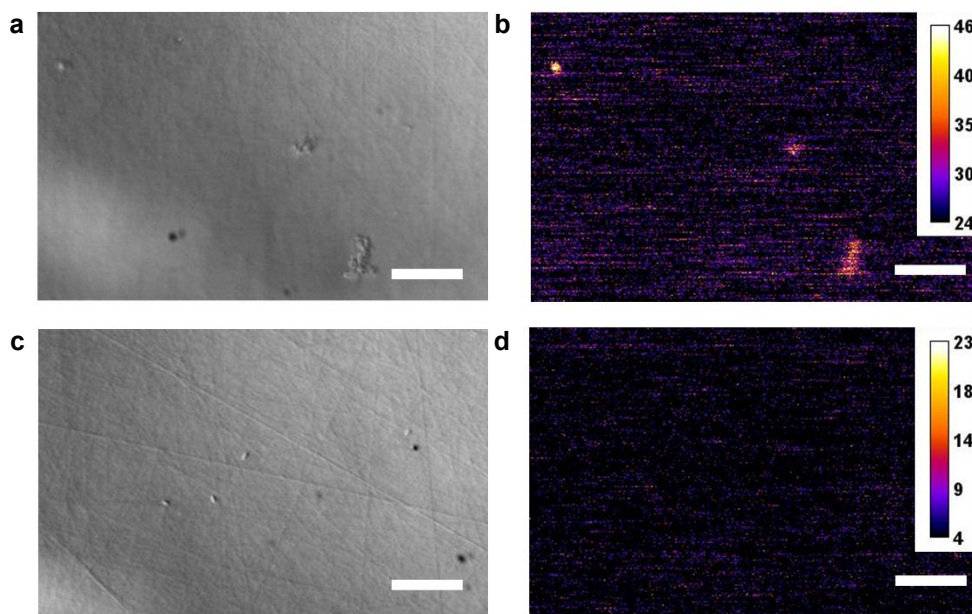
Figure S19. The corresponding BF image (a) and ECL image (b) of NCD/MSN. The corresponding BF image (c) and ECL image (d) of only MSN. Scale bar (white) is 20 μm. For ECL images, the exposure time is 500 ms, and the applied voltage is 1.2 V.
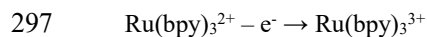
The FT-IR image of the synthetic NCDs was displayed in Figure S18c. The characteristic peaks of C≡C (2182.5 cm^{-1}) and aromatic ring (1632.9 and 767.0 cm^{-1}), N-H (3442.8 cm^{-1}) and C-H (2923.6 and 1463.7 cm^{-1}) indicate the successful synthesis of
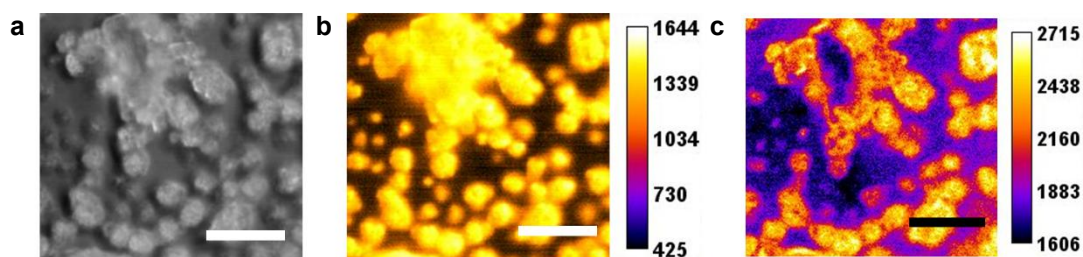
NCDs. Zeta potential was shown in Figure S18b, verifying the availability of electrostatic interaction between MSN and NCDs. The amino contents of NCDs were determined as 1693.71 μM/g by Kaiser agent (Figure S18e). According to the Stokes-Einstein equation (eq. S19), the diffusion coefficient of NCDs can be obtained, where r_i is the representative size of NCDs (3.2 nm) and η is 1 mPa·s for water under 293 K. Thus, D for NCDs was calculated as 6.7×10^{-11} m^2/s, while D for TPrA was 5×10^{-9} m^2/s in this context.

Because the abundant amino groups contained in NCDs could act as coreactants for Ru(bpy)$_3$$^{2+}$, the stable ECL emission of NCDs/MSN was gained in Figure S19b, while no ECL emission could be shown in only MSN without available amino groups (Figure S19d).

The possible mechanism of ECL emission between NCDs and Ru(bpy)$_3$$^{2+}$ could be represented below according to previous work[4]:

$$Ru(bpy)_3^{2+} - e^- \rightarrow Ru(bpy)_3^{3+}$$

$$NCDs - e^- \rightarrow NCDs^{\bullet+}$$

$$NCDs^{\bullet+} \rightarrow NCDs^{\bullet} + H+$$

$$Ru(bpy)_3^{3+} + NCDs^{\bullet} \rightarrow Ru(bpy)_3^{2+*}$$

$$Ru(bpy)_3^{2+*} \rightarrow Ru(bpy)_3^{2+} + hv$$
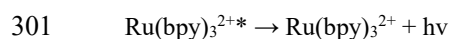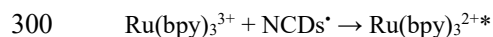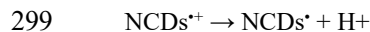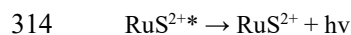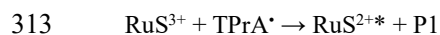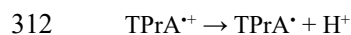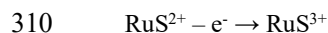

Figure S20. The corresponding BF image (a), FL image (b) and ECL image (c) of RuS. For FL image, the exposure time was 10 ms, and for ECL image, the exposure time was 200 ms. Scale bar (white and black) is 20 μm. For ECL image, the applied potential was 1.2 V.

To immobilize the luminophores, the RuS was prepared through a facile solvent evaporation method. Accordingly, a solution of 50 mM Ru(bpy)$_3$(PF$_6$)$_2$ in a mixed solvent of acetonitrile and n-propanol (5:1, v/v) was placed on the GCE surface. Then, RuS can be obtained on the electrode surface after natural air-drying. The RuS still exhibited the highest ECL emission at 1.2 V. Based on the previous report, the ECL pathway could be described below[12]:
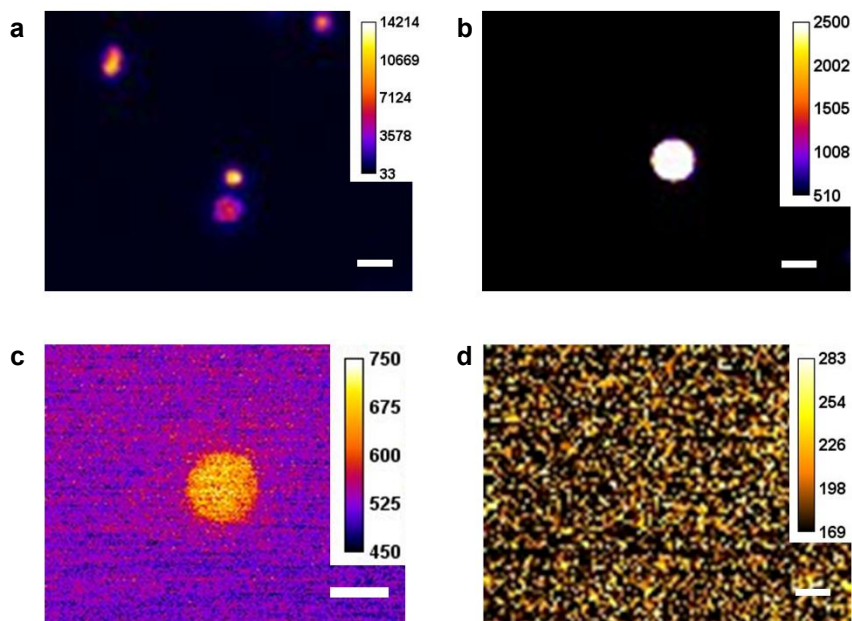
$$RuS^{2+} - e^- \rightarrow RuS^{3+}$$

$$TPrA - e^- \rightarrow TPrA^{\bullet+}$$

$$TPrA^{\bullet+} \rightarrow TPrA^{\bullet} + H^+$$

$$RuS^{3+} + TPrA^{\bullet} \rightarrow RuS^{2+*} + P1$$

$$RuS^{2+*} \rightarrow RuS^{2+} + hv$$

319

320

Figure S21. The corresponding FL images of $Ru(bpy)_3^{2+}$ labeled 1.5 μm SiO_2 beads (a), 5 μm SiO_2 bead (b) and 10 μm PS bead (c). Exposure time: 100 ms. Scale bar for (a), (b): 5 μm. Scale bar for (c): 10 μm. (d) The representative HT-ECL image at 0 V in 10 mM PBS (pH 7.4) containing 100 mM TPrA, indicating that the scatter of laser was not collected at camera parameters. Exposure time: 800 ms. Scale bar: 5 μm.
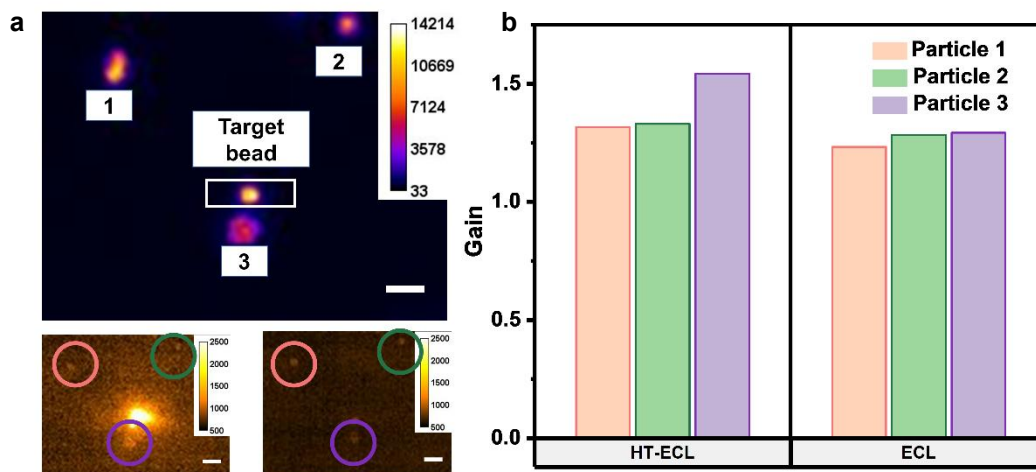
324

325

326

327

328
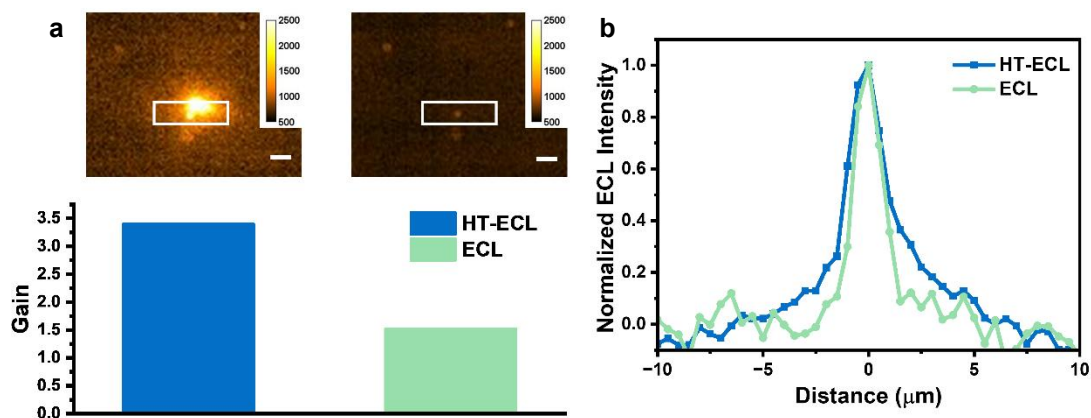
Figure S22. (a) Top: The corresponding HT-ECL image (left) and ECL image (right) for the same $Ru(bpy)_3^{2+}$ labeled 1.5 μm SiO_2 beads in 10 mM PBS (pH 7.4) containing 100 mM TPrA. The HT-ECL at the blank region partially submerges the target bead. Applied voltage: 1.3 V. Exposure time: 800 ms. Scale bar: 5 μm. Bottom: The corresponding HT-ECL and ECL gain for the target bead in the upper image. (b) The normalized ECL intensity along the white rectangular in the top image of (a).
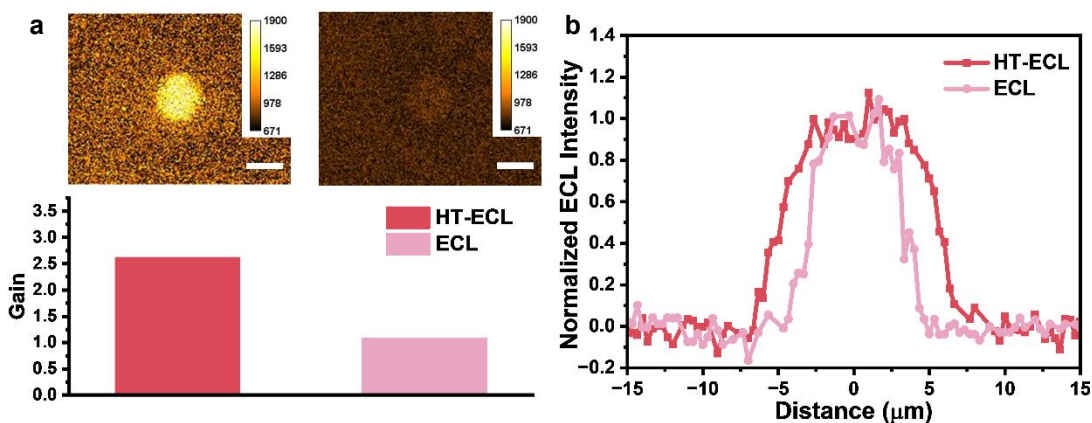
333

334

20

Figure S23. (a) Top: The FL image depicts 1.5 μm SiO2 beads labeled with $Ru(bpy)_3^{2+}$, with particles designated as 1, 2, and 3 positioned around the target bead. Bottom: The HT-ECL and ECL image of particle 1, 2, 3 in 10 mM PBS (pH 7.4) containing 100 mM TPrA. Applied voltage: 1.3 V. Exposure time: 800 ms. Scale bar: 5 μm. (b) The corresponding HT-ECL and ECL gain of particle 1, 2, and 3 in (a).
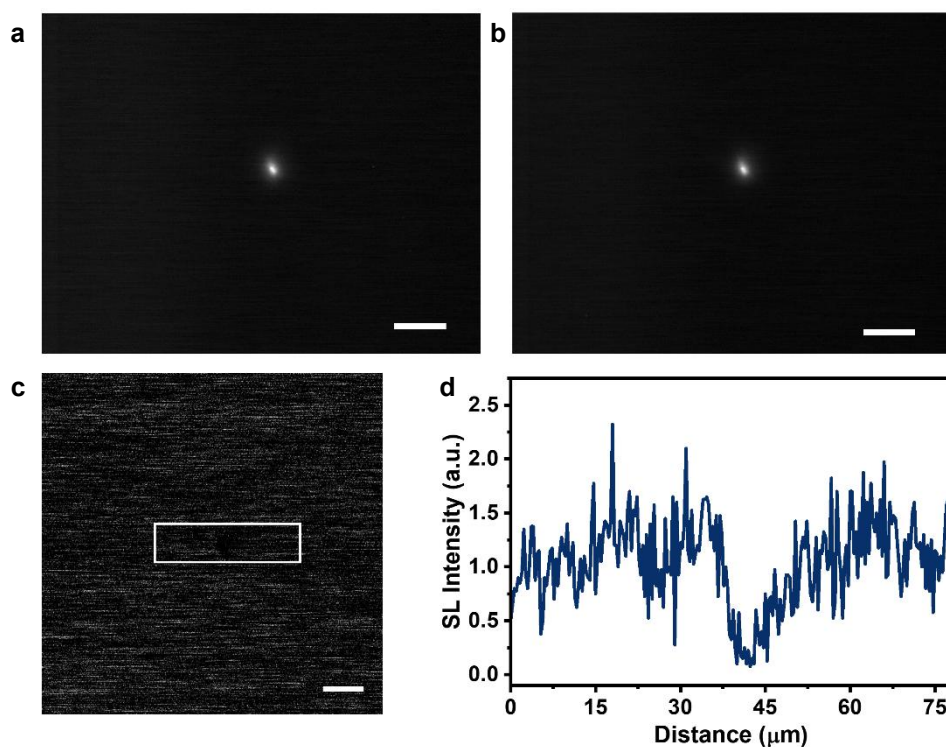
Figure S24. (a) Top: The corresponding HT-ECL image (left) and ECL image (right) for the same $Ru(bpy)_3^{2+}$ labeled 10 μm PS bead in 10 mM PBS (pH 7.4) containing 100 mM TPrA. Applied voltage: 1.3 V. Exposure time: 800 ms. Scale bar: 10 μm. Bottom: The corresponding HT-ECL and ECL gain for the target bead in the upper image. (b) The normalized ECL intensity along the radius of PS bead in (a).

Figure S25. (a) The overlay image of original 20 SL images without potential applied. (b) The overlay image of original 20 SL images when 1.4 V was applied. (c) Image obtained after subtracting (a) from (b). Scale bar (white) is 20 μm. Exposure time is 1 s. (d) The intensity analysis along the white rectangular in (c).

Figure S25 displayed the scattering light of laser on no-labeling CEM cells before and after imposing applied voltage. On the bare GCE surface, the scattering light of laser could totally not be recorded because of two short-pass 700 nm filters, but it may be recorded inevitably due to the CEM cell itself and the increasing collection parameters of EMCCD during the imaging of cell membrane. However, following the image processing steps mentioned in experimental sections, we observed that the pure scattering light intensity of laser at cell regions decreased with the increase in voltage, which could be ascribed to the electron loss process on the electrode surface. As shown in the Figure S25d, the intensity along the laser scattering spot indicated that the center region was weaker than the background, having no influence on our HT-ECL enhancement.
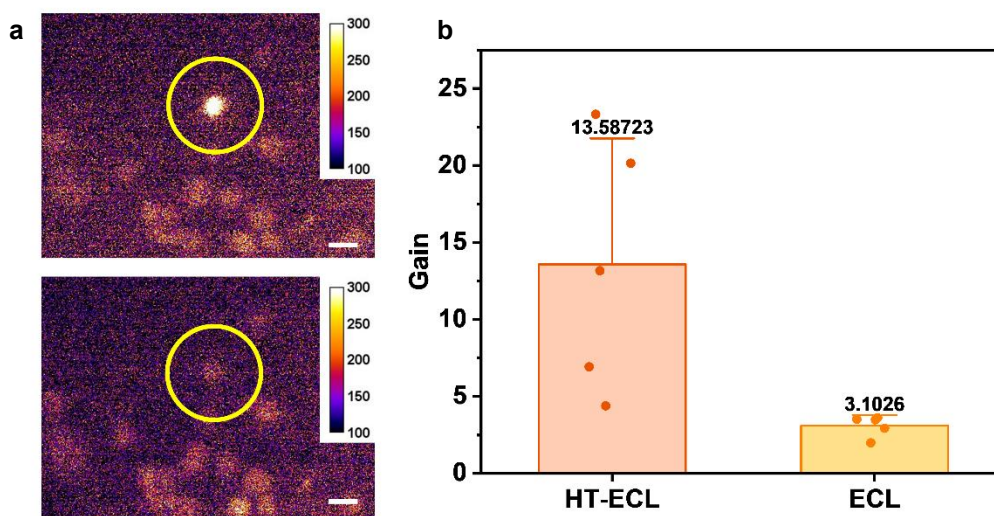
Figure S26. (a) The corresponding HT-ECL image (top) and ECL image (bottom) after image analysis. The yellow circle indicates the same MCF-7 cell with HT-ECL and without HT-ECL. Scale bar (white) is 20 μm. Exposure time is 1 s. (b) The statistic gain of HT-ECL (n=5) and ECL (n=5). The numbers indicate the average values of gain. The error bars suggest the standard deviation.

Reference

1   Valenti, G. *et al.* Single Cell Electrochemiluminescence Imaging: From the Proof-of-Concept to Disposable Device-Based Analysis. *J. Am. Chem. Soc.* **139**, 16830-16837, doi:10.1021/jacs.7b09260 (2017).

2   Ma, C. *et al.* Dynamically imaging collision electrochemistry of single electrochemiluminescence nano-emitters. *Chem. Sci.* **9**, 6167-6175, doi:10.1039/c8sc02251h (2018).

3   Liang, T. *et al.* Adapting and Remolding: Orchestrating Tumor Microenvironment Normalization with Photodynamic Therapy by Size Transformable Nanoframeworks. *Angew. Chem. Int. Ed. Engl.* **60**, 11464-11473, doi:10.1002/anie.202102180 (2021).

4   Ma, C. *et al.* Catalytic route electrochemiluminescence microscopy of cell membranes with nitrogen-doped carbon dots as nano-coreactants. *Chem Commun* **57**, 2168-2171, doi:10.1039/d0cc08223f (2021).

5   Giaccherini, A. *et al.* Analysis of mass transport in ionic liquids: a rotating disk electrode approach. *Scientific Reports* **10**, 13433, doi:10.1038/s41598-020-70301-w (2020).

6   Ishii, J. & Ono, A. A Fourier-transform spectrometer for accurate thermometric applications at low temperatures. *Aip Conf Proc* **684**, 705-710, doi:10.1063/1.1627210 (2003).

7   Voci, S., Al-Kutubi, H., Rassaei, L., Mathwig, K. & Sojic, N. Electrochemiluminescence reaction pathways in nanofluidic devices. *Anal Bioanal Chem* **412**, 4067-4075, doi:10.1007/s00216-020-02630-8 (2020).

8   Guo, W., Zhou, P., Sun, L., Ding, H. & Su, B. Microtube Electrodes for Imaging the Electrochemiluminescence Layer and Deciphering the Reaction Mechanism. *Angew. Chem. Int. Ed. Engl.* **60**, 2089-2093, doi:10.1002/anie.202012340 (2021).

9   Ma, C., Xing, Z., Gou, X., Jiang, L. P. & Zhu, J. J. A temperature-tuned electrochemiluminescence layer for reversibly imaging cell topography. *Chem. Sci.* **13**, 13938-13947, doi:10.1039/d2sc04944a (2022).

10   Bolletta, F. & Bonafede, S. Chemiluminescence and Electrochemiluminescence of Coordination-Compounds. *Pure. Appl. Chem.* **58**, 1229-1232, doi:10.1351/pac198658091229 (1986).

11   Toshimitsu, Y., Katayama, Y. & Miura, T. Electrode reactions of ruthenium–bipyridine complex in amide-type ionic liquids. *Electrochim. Acta* **82**, 43-47, doi:10.1016/j.electacta.2012.01.113 (2012).

12   Li, Q., Zheng, J. Y., Yan, Y., Zhao, Y. S. & Yao, J. Electrogenerated chemiluminescence of metal-organic complex nanowires: reduced graphene oxide enhancement and biosensing application. *Adv. Mater.* **24**, 4745-4749, doi:10.1002/adma.201201931 (2012).